Numerical Study of Quantum-Dot-Embedded Solar Cells

Chien-Chung Lin, Ming-Hsuan Tan, Che-Pin Tsai, Kuei-Ya Chuang, and T. S. Lay, *Member, IEEE*

***Abstract*—A quantum-dot-embedded solar cell model with antireflection coating is proposed and studied numerically. The device model was designed by using MATLAB coding. A proper inclusion of quantum-dot-enhanced carrier absorption was achieved through a modified absorption coefficient and a structure dependent carrier lifetime. The transmission matrix and quasi-drift diffusion method were applied to simulate the optical and electrical characteristics of the device. The experimental results were fitted first to validate the model and provide parameters for optimization. The final simulation showed that the power conversion efficiency (PCE) of an ideal InGaP/GaAs+InAs QD dual-junction cell could achieve 39.04%.**

***Index Terms*—Intermediate band solar cell (IBSC), photovoltaic cells, quantum dot, simulation, tandem cell, transmission matrix method.**

I. Introduction

SINCE the beginning of the 20th century, humankind has increasingly relied on energy provided by fossil fuel. The resulting global warming effect and the depletion of fossil fuel have been fervently debated and examined over the past decade. To reduce dependence on fossil fuel, alternative energy sources have attracted considerable attention recently. One such promising candidate is photovoltaic technology, which converts solar energy into electricity with a low environmental impact. The semiconductor-based solar cell has been representative of this technology because of its long history of research. Traditionally, a single-band-gap semiconductor material can provide as high as 44% of power conversion efficiency (PCE) in the ideal case [1]. Luque *et al.* claimed that an intermediate band solar cell (IBSC) can realize triple-band absorption with one junction, which is much easier and simpler than using a tandem multijunction solar cell. It can be calculated theoretically that a single junction with an intermediate band (IB) can achieve more than 60% efficiency to convert solar energy into electricity [2].

One of the most promising methods for implementing such an IBSC structure involves incorporating quantum-dot (QD) layers into solar cells. QDs have been crucial in optoelectronic applications because of its 3-D confinement and δ-like density of state that can produce a low-threshold and highly efficient laser [3]. Implementing these quantum mechanical structures into a traditional device requires a proper simulation method to estimate their effects. Most previous work, however, has not matched the theoretical calculation of real device measurements [2], [4], [5]. Therefore, this study proposes an integrated platform by combining the regular transmission matrix method [6], quasi-drift diffusion model [7], and IBSC-detailed balance model [2] to address more effectively both the optical field distribution in the multiple-layer situation and electrical properties of the QD-embedded structure in a single-junction p-i-n cell. An InAs QD structure, which is the most popular installation for GaAs-based solar cells [8]–[10], was applied in the theoretical calculation of this study.

The remainder of this paper explains in detail the fundamental theory and simulation modeling applied in this study. A numerical fit to actual QD solar cell measurements is provided to validate the proposed model. To extend the result further, an optimized single-junction GaAs/InAs QD and dual-junction tandem InGaP/GaAs/InAs QD cell were calculated. The PCE can achieve as high as 39.04% in the more simply structured dual-junction design, which is comparable to the triple-junction device. This study contends that this model can be highly useful for designers of next-generation high-efficiency solar cells.

II. Theory

This section introduces the theory used in the simulation. In addition to the regular carrier transport equations, several concepts are included: the transmission matrix method, collection probability, IBSC model, and saturation current model for IBSC. The software algorithm is also revealed at the end of this section.

A. Transmission Matrix Method

The transmission matrix method is used to calculate the spectral transmittance characteristics when light travels in a layered medium, and the results can be applied for the spectral reflection and transmission characteristics [6], [11], [12]. The model is based on the Fresnel reflection and general two-port transmission theory. The matrix between two interfaces can be written

Manuscript received December 1, 2012; revised January 11, 2013; accepted January 12, 2013. Date of publication February 1, 2013; date of current version May 13, 2013. This work was supported in part by the National Science Council under Grant NSC101-2221-E-009-046-MY3 and Grant NSC101-3113-E-005-003.

C. C. Lin, M. H. Tan, and C. P. Tsai are with the Institute of Photonic System, National Chiao Tung University, Tainan 711, Taiwan (e-mail: chienchunglin@faculty.nctu.edu.tw; evovss48@hotmail.com; it-is-me780405@hotmail.com).

K. Y. Chuang and T. S. Lay are with the Department of Electrical Engineering, National Chung Hsing University, Taichung 402, Taiwan (e-mail: m923050003@gmail.com; tslay@dragon.nchu.edu.tw).

Color versions of one or more of the figures in this paper are available online at http://ieeexplore.ieee.org.

Digital Object Identifier 10.1109/JSTQE.2013.2244563

1077-260X © 2013 IEEE

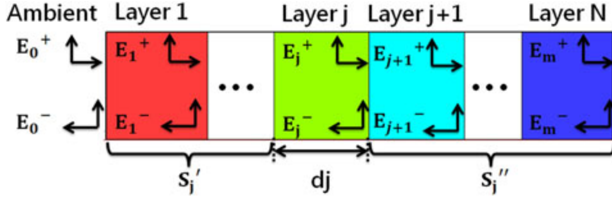

Fig. 1. EM wave propagation in a multiple layer system.

as

$$I_{j,j+1} = \frac{1}{t_{j,j+1}} \begin{bmatrix} 1 & r_{j,j+1} \\ r_{j,j+1} & 1 \end{bmatrix} \tag{1}$$

where $r_{j,j+1}$ and $t_{j,j+1}$ are the Fresnel complex reflection and transmission coefficients at the interface of layer j and $j+1$.

The layer matrix describing the propagation through layer j with thickness d_j is expressed as follows [6]:

$$L_j = \begin{bmatrix} e^{-i\zeta_j d_j} & 0 \\ 0 & e^{i\zeta_j d_j} \end{bmatrix} \tag{2}$$

where $\zeta_j = (2\pi/\lambda) \times q_j, q_j$, and d_j are complex propagation constant, complex refractive index, and thickness, respectively.

Considering a system with N layers, as shown in Fig. 1, to calculate the internal electric field in layer j, the entire matrix can be divided into two subsets, separated by layer j [6]:

$$S = \left(\prod_{v=1}^{N} I_{(v-1)v} L_v\right) \cdot I_{N(N+1)} = S'_j L_j S''_j \tag{3}$$

$$S'_j = \begin{bmatrix} S'_{j11} & S'_{j21} \\ S'_{j21} & S'_{j22} \end{bmatrix} = \left(\prod_{v=1}^{j-1} I_{(v-1)v} L_v\right) \cdot I_{(j-1)j} \tag{4}$$

$$S''_j = \begin{bmatrix} S''_{j11} & S''_{j21} \\ S''_{j21} & S''_{j22} \end{bmatrix} = \left(\prod_{v=j+1}^{N} I_{(v-1)v} L_v\right) \cdot I_{N(N+1)}. \tag{5}$$

By calculating the transmission matrix in each layer, the electric field intensity can be derived in any position [6]:

$$E_j(x) = \frac{S''_{j11} \cdot e^{-i\zeta_j (d_j - x)} + S''_{j21} \cdot e^{i\zeta_j (d_j - x)}}{S'_{j11} S''_{j11} \cdot e^{-i\zeta_j d_j} + S'_{j12} S''_{j21} \cdot e^{i\zeta_j d_j}} E_0^+. \tag{6}$$

The carrier generation rate by the unit time of a point x in the absorptive layer at different wavelength λ can be written as [6]

$$G(x) = \frac{1}{2} c\varepsilon_0 \alpha n \left|E(x)\right|^2 \tag{7}$$

where c is the speed of light, α is the absorption coefficient, $E(x)$ is the electric field distribution, ε_0 is the permittivity of free space, and n is the average refractive index.

B. Collection Probability

After the electron–hole pair is generated by a solar photon, the collection probability must be calculated to derive the short-circuit current (J_{SC}), because not every photogenerated carrier can reach the electrode and be drained as electrical output currents. To calculate the collection probability, the effective surface recombination rate for each junction must be specified. In the multiple-layered structure, as shown in Fig. 2, there are many interfaces with possible defects or traps to consume the carriers. By assuming a perfect collection in the depletion region (= 1), the combinational effect of multiple layers on the effective surface recombination rate can be given by [13]

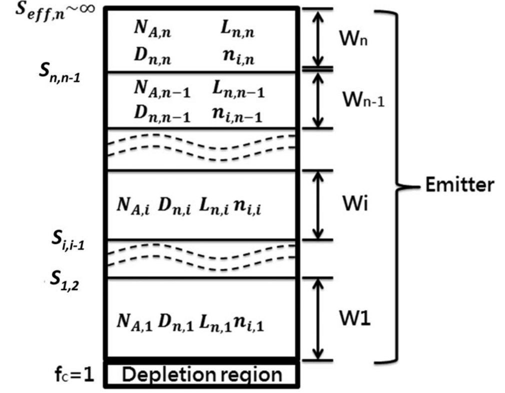

Fig. 2. Schematic representation for a multiple layer solar cell in P-region.

$$S_i^{\mathrm{eff}} = \frac{D_{i+1}}{L_{i+1}} \frac{N_{A,i}}{N_{A,i+1}} \left(\frac{n_{i,i+1}}{n_{i,i}}\right)^2 \times \frac{D_{i+1} \tanh(W_{i+1}/L_{i+1}) + S_{i+1}^{\mathrm{eff}} L_{i+1}}{D_{i+1} + \tanh(W_{i+1}/L_{i+1}) S_{i+1}^{\mathrm{eff}} L_{i+1}} + S_{i,i+1} \tag{8}$$

where D_i denotes the diffusion constant, L_i denotes the diffusion length for minority carriers, W_i is the width of the ith layer, S_i^{eff} is the effective back surface recombination rate in region i, and $S_{i,i+1}$ is the collective recombination velocity at the i and $i + 1$ heterojunction. Factors that affect the rate of the equivalent surface recombination include the difference of doping, intrinsic carrier concentration, diffusion constant, and band gap between materials [13].

After deriving the effective surface recombination rate for each junction, the collection probability can be calculated using the following algorithm [13]:

$$f_{c,i}(x) = f_{c,i-1}\Delta \tag{9}$$

$$\Delta = \frac{D_i \cosh\left(\frac{W_i - (x - x_i)}{L_i}\right) + S_i^{\mathrm{eff}} L_i \sinh\left(\frac{W_i - (x - x_i)}{L_i}\right)}{D_i \cosh\left(\frac{W_i}{L_i}\right) + S_i^{\mathrm{eff}} L_i \sinh\left(\frac{W_i}{L_i}\right)}. \tag{10}$$

The collection probability in the n-type region is determined similarly [13]. After the carrier generation rate and collection probability are known, the photogenerated current can be calculated using (11):

$$J_{\mathrm{photo}} = q \int_0^W G(x) f_c(x) dx \tag{11}$$

where W is the thickness of the solar cell and $f_c(x)$ is the location-dependent collection probability.

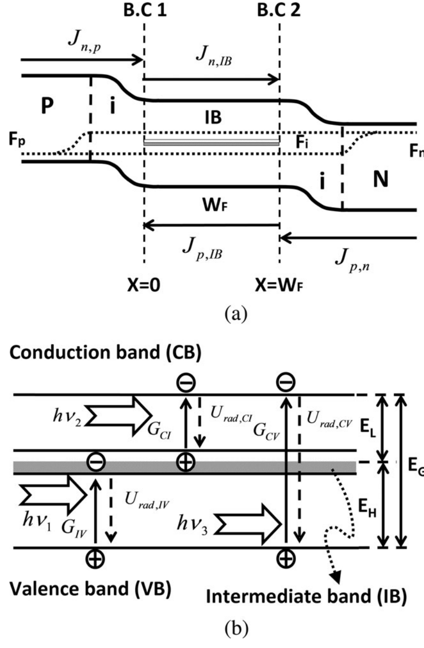

Fig. 3. (a) Band structure in forward bias of theIBSC. (b) Illustration of the generation and recombination processes in the QD–IB material.

C. Intermediate Band Solar Cell Model

The characteristics of the QD laser in the device must be properly evaluated. This QD layer can create the IB layer in the surrounding material band gap (in this case, GaAs), and the quasi-drift diffusion model can be applied [7], [14]. The band structure of the forward-biased IBSC is shown in Fig. 3(a). The complete IB can be assumed with no width in energy distribution, and a flat band is also imposed for simplicity of calculation.

The generation rates for the valence band to conduction band transitions $G_{\mathrm{CV}}(x)$, IB to conduction band transitions $G_{\mathrm{CI}}(x)$, and valence band to IB transitions $G_{\mathrm{IV}}(x)$ are considered first, as shown in Fig. 3(b) [7]

$$G_{\mathrm{CV}}(x) = \int_{E_G}^{\infty} [1 - R(E)] F(E) \alpha_{\mathrm{CV}}(E) e^{-\alpha_{\mathrm{CV}}(E)x} dE \qquad (12)$$

$$G_{\mathrm{CI}}(x) = \gamma \int_{E_L}^{E_H} [1 - R(E)] F(E) \alpha_{\mathrm{CI}}(E) e^{-\alpha_{\mathrm{CI}}(E)x} dE \qquad (13)$$

$$G_{\mathrm{IV}}(x) = \gamma \int_{E_H}^{E_G} [1 - R(E)] F(E) \alpha_{\mathrm{IV}}(E) e^{-\alpha_{\mathrm{IV}}(E)x} dE \qquad (14)$$

where $F(E)$ is the AM1.5 spectrum, [1-$R(E)$] is the ratio of incident light power arriving at $x = 0$, which can be calculated using the transmission matrix method, and the γ factor is the number describing the extent to which electrons are confined at the QDs, and is given by [15]

$$\gamma = \frac{3}{4}\pi \left(\frac{r_d}{d}\right)^3 \qquad (15)$$

where r_d is the radius of the QD and d is the distance between the dots.

Regarding the absorption coefficients of IB transitions, the truncated Lorentzian line shape is used as the basis of calculations. The absorption of the QD layer has been treated as Lorentzian in previous studies [16], [17]. To simplify the integral process, the absorption of QD can be chopped at the boundaries of photonic transition (i.e., valence to conduction, valence to IB, and IB to conduction) [2], [18].

Assuming only diffusion current in the flat band region where the IB material is embedded, as shown in Fig. 3. The electron and hole concentrations in the flat band region ($0 < x < W_F$) are given as [14]

$$D_{n,f} \frac{d^2 \Delta n}{dx^2} - U_{\mathrm{CV}} - U_{\mathrm{CI}} + G_{\mathrm{CV}} + G_{\mathrm{CI}} = 0 \qquad (16)$$

$$D_{p,f} \frac{d^2 \Delta p}{dx^2} - U_{\mathrm{CV}} - U_{\mathrm{IV}} + G_{\mathrm{CV}} + G_{\mathrm{IV}} = 0 \qquad (17)$$

where $D_{n,f}$ and $D_{p,f}$ are the carrier diffusion constants. U_{CV}, U_{CI}, and U_{IV} are the excess radiative recombination rates among conduction, intermediate, and valence bands, respectively, as defined in [7], [14], and [15].

At thermal equilibrium, (16) and (17) can be solved analytically under the boundary conditions, as shown in Fig. 3(a) [14]

$$\text{B .C 1: } D_{n,f} \frac{d\Delta n}{dx} = \frac{1}{q} J_{n,p} \quad \text{for } x = 0 \qquad (18)$$

$$\text{B .C 2: } -D_{p,f} \frac{d\Delta p}{dx} = \frac{1}{q} J_{p,n} \quad \text{for } x = W_F. \qquad (19)$$

$J_{n,p}$ is the electron current from the p-layer, and $J_{p,n}$ is the hole current from the n-layer. Both $J_{n,p}$ and $J_{p,n}$ are solved using the transmission matrix and collection probability model introduced in Sections II-A and II-B. The hole-current density at thermal equilibrium in the flat band region is then given by [14]

$$\begin{aligned} J_{p,IB}(x=0) &= \int_{E_H}^{E_G} T_{\mathrm{top}\to IB} \cdot \left[\frac{\alpha_{\mathrm{IV}} L_h}{(\alpha_{\mathrm{IV}}^2 L_h^2 - 1)}\right] \\ &\quad \times \left\{ \frac{\alpha_{\mathrm{IV}} L_h e^{-\alpha_{\mathrm{IV}} W_F} + \sinh\left(\frac{W_F}{L_h}\right)}{\cosh\left(\frac{W_F}{L_h}\right)} - \alpha_{\mathrm{IV}} L_h \right\} dE \\ &\quad + \int_{E_G}^{\infty} T_{\mathrm{top}\to IB} \cdot \left[\frac{\alpha_{\mathrm{CV}} L_h}{(\alpha_{\mathrm{CV}}^2 L_h^2 - 1)}\right] \\ &\quad \times \left\{ \frac{\alpha_{\mathrm{CV}} L_h e^{-\alpha_{\mathrm{CV}} W_F} + \sinh\left(\frac{W_F}{L_h}\right)}{\cosh\left(\frac{W_F}{L_h}\right)} - \alpha_{\mathrm{CV}} L_h \right\} dE \\ &\quad + \frac{J_{p,n}}{\cosh\left(\frac{W_F}{L_h}\right)}. \end{aligned} \qquad (20)$$

The electron current density at thermal equilibrium in the flat band region is given by [14]

$$\begin{aligned} J_{n,IB}(x=W_F) &= \int_{E_L}^{E_H} T_{\mathrm{top}\to IB} \cdot \left[\frac{\alpha_{\mathrm{CI}} L_e}{(\alpha_{\mathrm{CI}}^2 L_e^2 - 1)}\right] \\ &\quad \times \left\{ \frac{e^{-\alpha_{\mathrm{CI}} W_F} \sinh\left(\frac{W_F}{L_e}\right) - \alpha_{\mathrm{CI}} L_e}{\cosh\left(\frac{W_F}{L_e}\right)} + \alpha_{\mathrm{CI}} L_e e^{-\alpha_{\mathrm{CI}} W_F} \right\} dE \\ &\quad + \int_{E_H}^{\infty} T_{\mathrm{top}\to IB} \cdot \left[\frac{\alpha_{\mathrm{CV}} L_e}{(\alpha_{\mathrm{CV}}^2 L_e^2 - 1)}\right] \end{aligned}$$

$$\times \left\{ \frac{e^{-\alpha_{\mathrm{CV}} W_F} \sinh\left(\frac{W_F}{L_e}\right) - \alpha_{\mathrm{CV}} L_e}{\cosh\left(\frac{W_F}{L_e}\right)} + \alpha_{\mathrm{CV}} L_e e^{-\alpha_{\mathrm{CV}} W_F} \right\} dE + \frac{J_{n,p}}{\cosh\left(\frac{W_F}{L_e}\right)} \tag{21}$$

where $T_{\mathrm{top}\to IB}$ is the ratio of incident light power arriving at $x = 0$, and L_e and L_h are the diffusion lengths of the electron and hole in the flat band region, as defined in [14].

Finally, the total short-circuit current density J_{SC} can be contained at thermal equilibrium

$$J_{\mathrm{SC}} = -(J_{n,p} + J_{p,IB}) = -(J_{p,n} + J_{n,IB}) \tag{22}$$

and the currents extracted from both of the terminals must be equal.

D. Saturation Current Model

The saturation current J_0 is critical when determining the *I–V* characteristics of a diode, and it can be divided into four components: the first from the edge of the depletion layers ($J_{s,\mathrm{bulk}}$); the second from the radiative band-to-band recombination current density ($J_{r,\mathrm{CV}}$); the third from the radiative recombination current density because of the IB ($J_{r,\mathrm{CI}}$); and finally, the fourth from the nonradiative recombination current density (J_{nr}). At the end, the overall result is $J_0 = J_{s,\mathrm{bulk}} + J_{r,\mathrm{CV}} + J_{r,\mathrm{CI}} + J_{\mathrm{nr}}$.

The first component of J_0 can be written in the form of [19]

$$J_{s,\mathrm{bulk}} = \left\{ \frac{q \cdot n_i^2 \cdot D_n}{L_n \cdot N_a} \left[\frac{\frac{S_n \cdot L_n}{D_n} \cosh\left(\frac{Z_p}{L_n}\right) + \sinh\left(\frac{Z_p}{L_n}\right)}{\frac{S_n \cdot L_n}{D_n} \sinh\left(\frac{Z_p}{L_n}\right) + \cosh\left(\frac{Z_p}{L_n}\right)} \right] + \frac{q \cdot n_i^2 \cdot D_p}{L_p \cdot N_d} \left[\frac{\frac{S_p \cdot L_p}{D_p} \cosh\left(\frac{Z_n}{L_p}\right) + \sinh\left(\frac{Z_n}{L_p}\right)}{\frac{S_p \cdot L_p}{D_p} \sinh\left(\frac{Z_n}{L_p}\right) + \cosh\left(\frac{Z_n}{L_p}\right)} \right] \right\} \times \left[\exp\left(\frac{qV_A}{kT}\right) - 1 \right] \tag{23}$$

where $n_i^2 = N_C.\ N_V.\exp(-E_{\mathrm{g,bulk}}/\mathrm{KT})$, N_C and N_v are the effective densities of state in the bulk materials, N_d and N_a are the donor and acceptor concentrations in the n-type and p-type regions, S_p and S_n are the effective surface recombination rates in the n-type and p-type regions, D_n and D_p are the diffusion constants, L_n and L_p are the diffusion lengths, Z_n and Z_p are the thicknesses of the *n*-type and p-type regions, respectively, and V_A is the applied bias.

The second component of J_0 can be written in the form of [20]

$$J_{r,CV} = q \frac{2\pi}{h^3 c^2} \int_{EG}^{\infty} e^{\left(\frac{-E}{KT}\right)} \cdot E^2 (1 - e^{(-\alpha_{\mathrm{CV}} W_F)}) dE \times \left[\exp\left(\frac{qV_A}{kT}\right) - 1 \right]. \tag{24}$$

The third component of J_0 can be described by [20]

$$\begin{aligned} J_{r,\mathrm{CI}} &= J_{0,r,\mathrm{CI}} \left[\exp\left(\frac{qV_A(1-\zeta)}{kT}\right) - 1 \right] \\ &= J_{0,r,\mathrm{IV}} \left[\exp\left(\frac{q\mu_{\mathrm{IV}}}{kT}\right) - 1 \right] \\ &= J_{0,r,\mathrm{IV}} \left[\exp\left(\frac{qV_A \zeta}{kT}\right) - 1 \right] = J_{r,IV} \end{aligned} \tag{25a}$$

where

$$J_{r,\mathrm{CI}} = q \frac{2\pi}{h^3 c^2} \int_{E_L}^{E_H} e^{\left(\frac{-E}{KT}\right)} \cdot E^2 (1 - e^{(-\alpha_{\mathrm{CI}} W_F)}) dE \tag{25b}$$

$$J_{r,\mathrm{IV}} = q \frac{2\pi}{h^3 c^2} \int_{E_H}^{E_G} e^{\left(\frac{-E}{KT}\right)} \cdot E^2 (1 - e^{(-\alpha_{\mathrm{IV}} W_F)}) dE \tag{25c}$$

and μ_{CI} represents the splitting of the Fermi level between CB and IB. Equation (25a) can be used to solve ζ by matching the electron and hole recombination current density through the IB in the dark.

The final component of J_0 can be written in [20]

$$J_{\mathrm{nr}} = q \cdot n_{i,\mathrm{bulk}} \frac{W}{\tau_{\mathrm{SRH}}} \times \left[\exp\left(\frac{qV_A}{kT}\right) - 1 \right] \tag{26}$$

where $n_{i,\mathrm{bulk}}$ is the intrinsic concentration, and W and τ_{SRH} are the width and the carrier nonradiative recombination lifetime in i-layer, respectively. By summing (23), (24), (25a), and (26), the total J_0 can be determined.

E. Quantum-Dot Layer Number and Spacer Thickness

The epitaxial structure of the QD region is a key component in the proposed solar cell design. It dominates the long-wavelength absorption and also the source of the nonradiative recombination. The lattice mismatch between InAs and GaAs naturally introduces stress between the dots and the substrate. When the QD layers are grown in succession, this stress can accumulate along the growth until it is large enough to break the atomic bond and defects are created. The amount of stress can be tuned by the number of QD layers and the distance, that is, the GaAs spacer thickness, between the QD layers. Many past research results have been focused on the strain-balanced QD growth to increase the stacked number of QD layers [21], [22]. By contrast, the spacer thickness can play a critical role in shaping the individual QD layers and the stress around them [23], [24].

The influences of these parameters (GaAs spacer thickness and QD layer numbers) can be seen in the diode $J_{\mathrm{sc}}-V_{\mathrm{oc}}$ measurement through the changes in the carrier lifetime in (26). In the proposed model, it is important to develop a feasible way to predict the carrier lifetime as the function of spacer thickness (T_{spacer}) and layer number (N_{layer}). Based on measuring the devices, the following expression is suitable for fitting:

$$\tau_{\mathrm{eff}} = A \times \log(T_{\mathrm{spacer}}) \times (N_{\mathrm{layer}})^{-B} + \tau_{\mathrm{const}} \tag{27}$$

where A, B, and τ_{const} are the fitting parameters. Based on the fitting parameters, this model could be extended to different spacer thicknesses or QD layer numbers. Fig. 4 shows the mapping of carrier lifetime under different spacer thicknesses

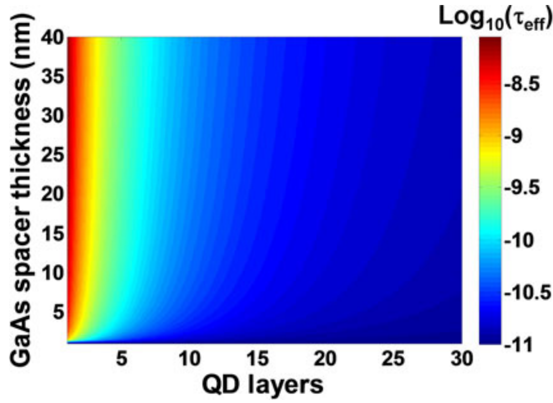

Fig. 4. Calculated carrier lifetime according to our device result.

and layer numbers. A dramatic reduction of the carrier lifetime can lead to the reduction of open-circuit voltages through the dark current formation [25]. Based on the results from the other group, a similar trend of carrier lifetime can be found, and they are generally in the range of 10^{-9} s at a high stacking number of QD layers [21], [26]. The implication of the differences in lifetime is the design variation of the QD epitaxial structure. The closer the QD layer, the higher the tunneling current that is caused by the stronger coupling of quantum mechanical wave functions. This tunneling effect can reduce the probability of the carrier to remain in the IB, thus lowering the efficiency [27], [28]. Other than tunneling, the strain developed in the epitaxial layer could cause further defect propagation across the structure, which can serve as a nonradiative recombination center to consume the photogenerated electrons and holes. Hence, closer InAs quantum layers and more stacked QD layers lead to a shorter carrier lifetime, as demonstrated in the proposed current device and model. Although the high layer number is relatively helpful in boosting efficiency, the defects, and traps that accompany this design might offset all of the effort expended to increase the absorption, and the short-circuit currents suffer substantially from this recombination; thus, the efficiency of QD solar cells cannot be improved.

Both factors (QD layer number and GaAs spacer) are crucial in fabricating a successful QD-embedded solar cell. These highlights will be properly placed in the original paper (please see the following paragraph). The strain-compensated design of the QD layer will become valuable for the future development of highly efficient IBSCs.

F. I–V Characteristics

Fig. 5 illustrates the flowchart of the proposed model. First, the device structure is set up, and initial parameters are inputted into the program. Thereafter, the corresponding transmission matrix and collection probability calculations are conducted, and the effective surface recombination rate can be found. The continuity equations are then solved for $J_{\rm sc}$, and the IB transition restrain $(J_{\rm s,CI} = J_{s,\rm IV})$ must be complied.

The total diode current density is determined according to the sum of the dark current and photocurrent resulting from the valence to conduction band and IB radiative transitions:

$$J(V) = J_{\rm SC} - J_0(V) \tag{28}$$

and the PCE of the solar cell is calculated as

$$\eta = \frac{J_{\rm SC} V_{\rm OC} FF}{P_{\rm Sun}} \tag{29}$$

where $V_{\rm OC}$ is the open-circuit voltage, $P_{\rm Sun}$ is the solar irradiance, and $FF = J_m {\rm V}_m/{\rm J}_{\rm SC} V_{\rm OC}$ is the fill factor. J_m and V_m are the current density and voltage, respectively, at the operating point where the power output from the solar cell is the maximum. Finally, EQE and *IV* can be outputted to match the experimental results, and the decision for the subsequent run parameter can be made.

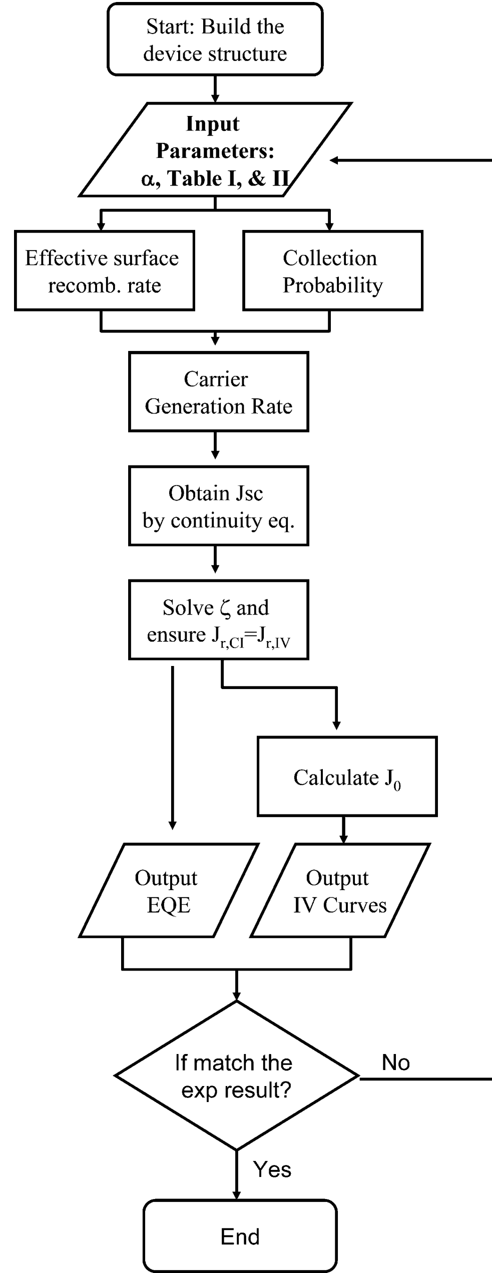

Fig. 5. Illustration of the solution process.

TABLE I
EPITAXIAL STRUCTURE OF A QD-EMBEDDED SOLAR CELL [37]

Quantum dot solar cell sample structure		Doping (cm^{-3})	Thickness(d) nm
AR-coating	SiO_2		100
P-layer	$Al_{0.5}Ga_{0.5}As$	2e18	400
	GaAs	2e17	50
I-layer	GaAs		200
×9	Cap-$In_{0.1}Ga_{0.9}As$ QD- $In_{0.75}Ga_{0.25}As$		10
	GaAs spacer		5&15
I-layer	GaAs		200
N-layer	$Al_{0.5}Ga_{0.5}As$	2e18	500
	GaAs	2e18	500

TABLE II
SIMULATION PARAMETERS

Symbol	parameter	Parameter with units
n	Ideal Factor	1.3
Rs	Series Resistance	2.58 Ω
Rsh	Shunt Resistance	3.86 kΩ
τ_{SRH}	Non-radiative carrier lifetime	1E-9 s
T	Temperature	300 K
E_H [31]	Band-gap between IB and VB	1 eV
E_L [31]	Band-gap between IB and CB	0.43 eV
E_G	Band-gap between CB and VB	1.43 eV
D_n(GaAs)	Diffusion constant of electrons	220.15 cm^2/s
D_p(GaAs)	Diffusion constant of holes	10.36 cm^2/s
$D_n(Al_{0.5}Ga_{0.5}As)$	Diffusion constant of electrons	3.75 cm^2/s
$D_p(Al_{0.5}Ga_{0.5}As)$	Diffusion constant of holes	2.07 cm^2/s

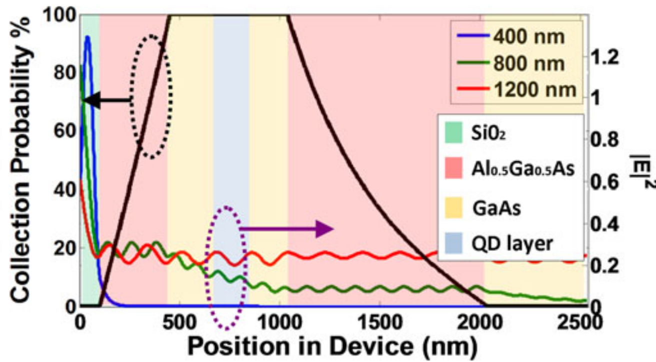

Fig. 6. Incident optical field intensity distribution (colored) and collection probability (black) in device (5 nm GaAs spacer).

III. VALIDATION OF THE MODEL TO SINGLE-JUNCTION QD SOLAR CELLS

A single-junction GaAs/AlGaAs/InGaAs QD solar cell device (shown in Table I) was grown in a previous study by using a molecular beam epitaxial system [29], and a regular process was conducted for device fabrication. The epitaxial structure is not optimized for a photovoltaic response; hence, the efficiency is not high. By using the proposed model, the IV and EQE can be fitted by one set of parameters listed in Table II. The incident optical field intensity distribution and the calculated collection probability are shown in Fig. 6. By adjusting the proper surface

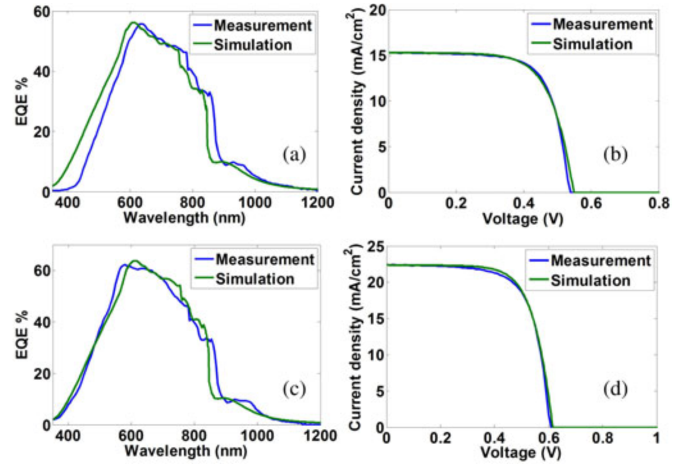

Fig. 7. Comparison of calculated and measured EQE / I–V characteristics of GaAs solar cell with QD by MATLAB: (a), (b) for 5 nm GaAs spacer and (c),(d) for 15 nm GaAs spacer.

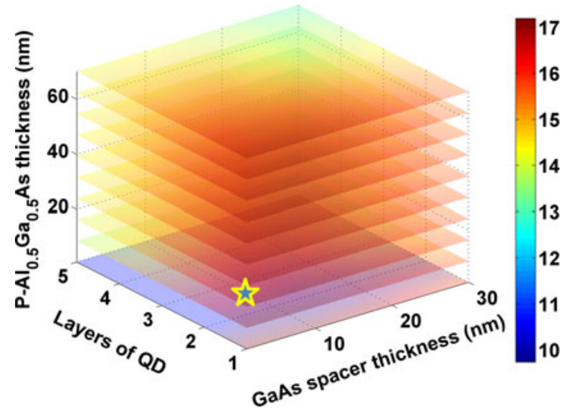

Fig. 8. Calculation of PCE with tuning the thickness of p-AlGaAs, GaAs spacer and QD layers, and the color bar is efficiency in percentage.

recombination velocity (9×10^8 cm/s), as well as the absorption coefficients of materials [30], the *IV* and EQE fitting can be obtained, as shown in Fig. 7.

Although the experimental data are properly fitted, the optimized design for the QD-embedded device has yet to be found. In the simulation conducted in this study, the thicknesses of p-AlGaAs, the GaAs-spacer, and QD layer numbers could be varied to determine the best combination, the results of which are shown three-dimensionally in Fig. 8. As indicated by the location of the cursor in the plot, the best PCE appears at p-AlGaAs = 16.33 nm, with 1 QD layers, and the PCE can achieve 17.18%. Comparing the baseline structure with GaAs in the intrinsic region, in which PCE can achieve 16.54%, shows that the QD structure may have a lower open-circuit voltage but obtains a higher short-circuit current when the thicknesses of the device are optimized. The calculated EQE and *IV* curves are shown in Fig. 9. The reduction of the carrier lifetime when QD layer number increases, as pointed out in Section II, is the main reason that the maximum efficiency happens at 1 QD layer design. These simulation results demonstrate the enhancement by including

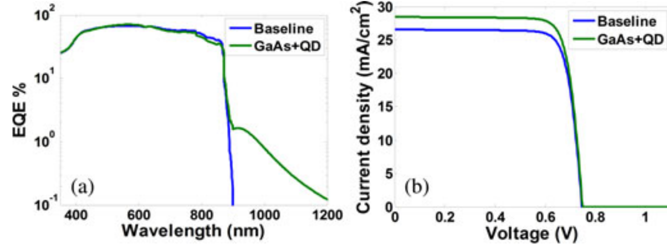

Fig. 9. Comparison of GaAs baseline and QD embedded device: (a) EQE and (b) IV. Both devices are based on the AlGaAs/GaAs structure developed in Table I.

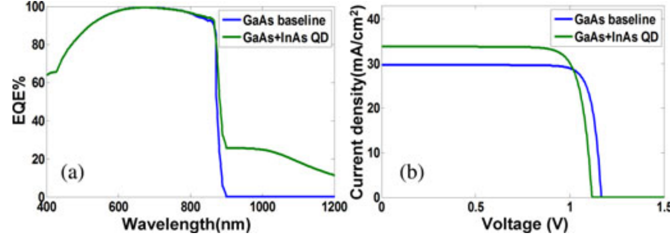

Fig. 10. Comparison of GaAs baseline and optimized QD embedded device: (a) EQE and (b) IV.

the QD layers, and the PCE of the devices can be improved by as high as 3.87%.

IV. Optimization of a Single-Junction Device

The feasibility of the model was demonstrated by comparing the measurement data provided in Section III. In this section, the optimization of an ideal GaAs and InGaP single-junction cell is implemented. The resultant structures can be the foundation of a future study goal: the dual-junction QD-embedded cell. The GaAs cell can incorporate the QD layers to enhance the efficiency. The characteristics of QD and GaAs layers can be built reliably from the parameters in the previous section.

A. *GaAs Single-Junction Solar Cell*

GaAs is one of the most popular materials for single-junction solar cells because its direct band gap is nearly ideal, and the theoretical PCE can achieve 32% [1]. To optimize a GaAs single-junction p-i-n solar cell, an ideal antireflection coating is applied, the shading effect by the surface contact is ignored, and the nonradiative carrier lifetime for undoped GaAs is set for 15 ns [32]. Based on the proposed calculation algorithm, under a thin p-type emitter condition, the best pure GaAs solar cell appears at I–GaAs = 1921 nm with a fixed thickness of 3000 nm for the N-layer, and the PCE can achieve 30.56%. The QD layers are then added to complete the design. Two types of carrier lifetimes are adapted: the first type is the ideal case in which the quantum dot insertion does not affect the carrier lifetime (τ_{eff} = constant = 15 ns); the second type is the fitted lifetime by (27) from our devices. In the first case, the maximum efficiency of QD solar cell occurs at two layers of QD, and is independent of GaAs spacer thickness. The IV/EQE of GaAs p-i-n solar cells with and without QDs are both graphed as shown in Fig. 10. The PCE enhancement by including the QD layers is clear, and the efficiency can be improved from 30.56% to 30.74%.

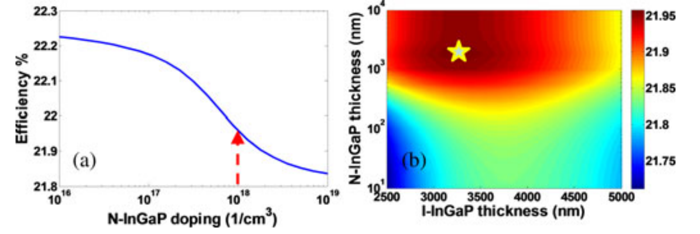

Fig. 11. (a) PCE with different N–InGaP doping concentration in the single-junction case. The red arrow indicates the efficiency at 10^{18} cm^{-3} doping concentration. (b) PCE of a single-junction InGaP solar cell with different N-InGaP and I-InGaP thicknesses. The doping concentration is 10^{18} cm^{-3} in this case.

In the second case, the dramatic drop in the carrier lifetime as the spacer thickness gets narrower and QD layer number climbs up. The photo-generated carrier loss due to tunneling and nonradiative recombination grows larger and thus the open-circuit voltage is greatly reduced. The best result occurs at single QD layer with 29.35% PCE, which is lower than the baseline and consistent with our observation in the experiments.

B. *InGaP Single-Junction Solar Cell*

Lattice-matched $In_{0.5}Ga_{0.5}P$ has played an essential role in multijunction tandem solar cells [33]–[35]. This material has a larger band gap of 1.9 eV; thus, it is a suitable choice for top cells in multijunction designs. To derive the high-efficiency tandem $In_{0.5}Ga_{0.5}P$/GaAs+InAs QD cell, the ideal structure for the $In_{0.5}Ga_{0.5}P$ p-i-n solar cell must be calculated first. Similar assumptions are made, as in the previous section, except that the nonradiative carrier lifetime of undoped $In_{0.5}Ga_{0.5}P$ is 1 ns [36].

The PCE dependence on n-type InGaP doping concentration can be calculated as shown in Fig. 11(a), which gives a variation of 22.02% $\pm$ 0.175%. This variation is small enough such that we will take a constant doping of 10^{18} cm^{-3} in the later program to reduce the computing time. On the other hand, the thickness of the n-type InGaP layer can also affect the efficiency of the solar cell. The 2-D contour plot can be seen in Fig. 11(b), and the maximum PCE of 21.96% can be found at 1584 nm for n-type layer thickness at the doping concentration of 10^{18} cm^{-3}.

V. Dual-Junction Device

After optimizing the single-junction device, the dual-junction device design can be undertaken. In the past, triple-junction devices have been fabricated, and their PCE was as high as 40% [37]. However, the growth of such devices is relatively complicated, which might be unsuitable for large-scale commercialization. Conversely, dual-junction devices are easier to fabricate, and by adding a QD layer, obtaining three absorption bands in a dual-junction scheme is possible. In the design shown in Fig. 12, the top and bottom cells are composed of InGaP and GaAs/QD, respectively. Between the cells, a highly doped tunnel junction is installed to connect both sides electronically.

The optimized design for each cell (top and bottom) has been demonstrated in the previous section. However, if the optimized structures are simply imported from previous sections, the current mismatch would lead to a lower PCE of 33.79%. Only when

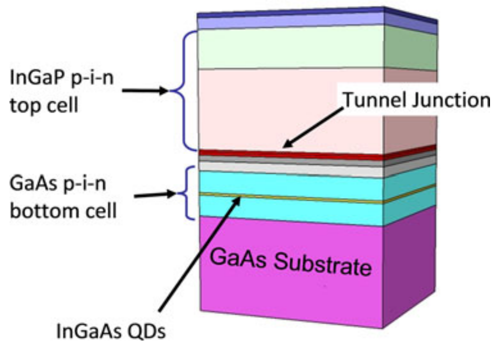

Fig. 12. InGaP/GaAs QD tandem solar cell schematic diagram.

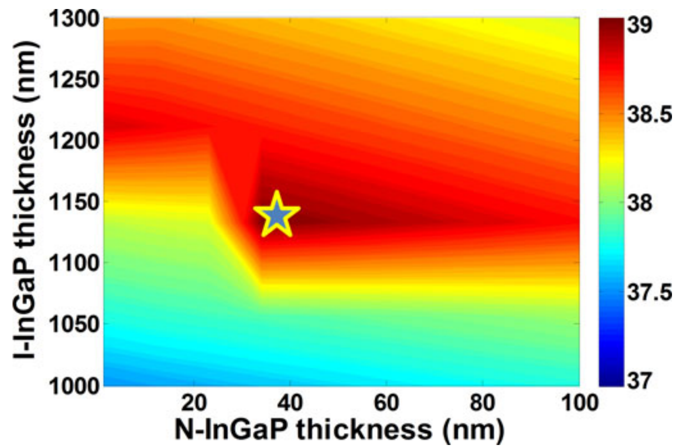

Fig. 13. Calculation of PCE with tuning the thickness of I–InGaP and N–InGaP for the ideal InGaP/GaAs+InAs QD dual junction solar cell.

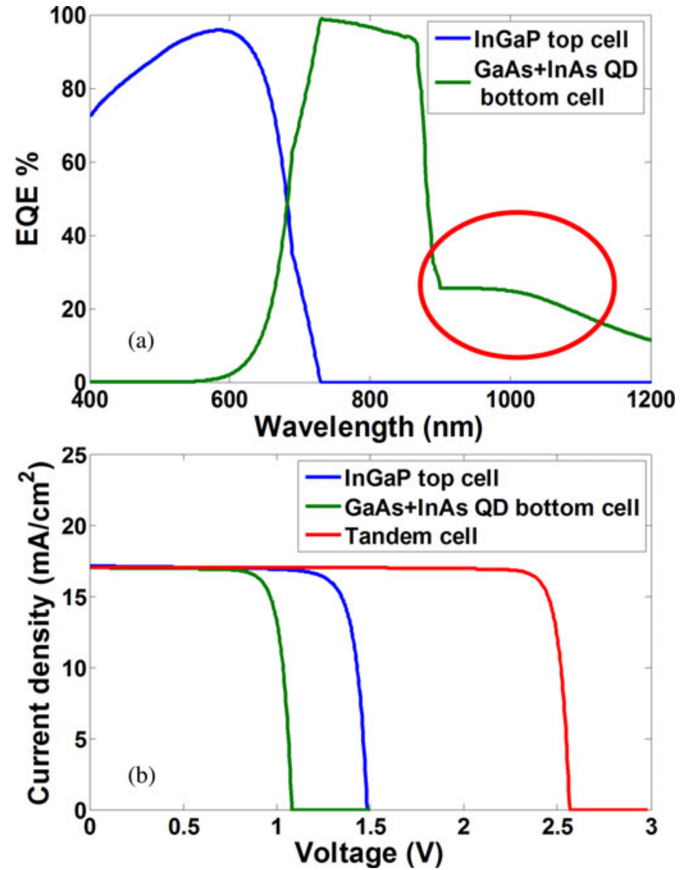

Fig. 14. Current-matched tandem cell with a QD layer simulated by MATLAB (a) EQE versus wavelength, the red circle marks the quantum dot contribution. (b) IV curves.

short-circuit currents are the same in both cells can the highest PCE be achieved.

Matching the top and bottom cell currents can be accomplished by varying the thicknesses of the I-InGaP and N-InGaP layers, with a thin p-type emitter at the top and the GaAs+InAs QD bottom cell, which is optimized in Section IV.A. Based on the proposed algorithm, the PCE can be mapped, as shown in Fig. 13. Since the n-type layer of InGaP in the tandem cell is thin due to the current matching, the doping concentration dependence is minimal in our current design. In this dual junction device, three different carrier lifetimes are tested: the first one is the ideal condition with constant carrier lifetime and strong QD absorption; the second one is the carrier lifetime from our devices fitted by (27); and the third one is the carrier lifetime extracted from [26]. Due to the deterioration of the carrier lifetime caused by either high layer number or small GaAs spacer, the second and third case can only yield 34.75% and 35.80% of PCE, respectively.

The best PCE appears in the first case at I-InGaP = 1133 nm and N-InGaP = 34 nm, and the PCE can achieve 39.04%. The IV/EQE plots are shown in Fig. 14, and the IV curve shows that both $V_{\rm oc}$ and $J_{\rm sc}$ of the tandem cell are enhanced when the diode current is matched.

This result, although not as favorable as 56% in the ideal triple-junction device [38], still surpasses the 35% efficiency in a previous dual-junction design [39], and could be a promising candidate for the cost-effective design of highly efficient solar cells. From the simulation, the importance of the carrier lifetime should be also fully recognized. Only when there is a good QD layer growth, there is a possibility to achieve high carrier lifetime, and thus high conversion efficiency.

VI. Conclusion

In conclusion, this study proposes a solar cell design that was analyzed systematically by combining the merits of QD IB absorption and a dual-junction tandem cell. This concept was applied on a MATLAB platform, and several models were integrated. By fitting the actual QD solar cells, the device parameters can be determined and used for forecasting the optimized structures. The final results showed that the proposed device can achieve a PCE as high as 39.04% under ideal condition. The proposed dual-junction QD-embedded solar cell is both easy to manufacture and highly efficient, and could be a promising design for next-generation photovoltaic devices.

References

[1] W. Shockley and H. J. Queisser, “Detailed balance limit of efficiency of p-n junction solar cells,” *J. Appl. Phys.*, vol. 32, no. 3, pp. 510–519, Mar. 1961.

[2] A. Luque and A. Martı, “Increasing the efficiency of ideal solar cells by photon induced transitions at intermediate levels,” *Phys. Rev. Lett.*, vol. 78, no. 26, pp. 5014–5017, Jun. 1997.

[3] D. L. Huffaker, G. Park, Z. Zou, O. B. Shchekin, and D. G. Deppe, “1.3 μm room-temperature GaAs-based quantum-dot laser,” *Appl. Phys. Lett.*, vol. 73, no. 18, pp. 2564–2566, Nov. 1998.

[4] L. Cuadra, A. Marti, and A. Luque, “Present status of intermediate band solar cell research,” *Thin Solid Films*, vol. 451–452, pp. 593–599, Mar. 2004.

[5] A. Luque, A. Marti, N. López, E. Antolín, and E. Cánovas, “Operation of the intermediate band solar cell under non-ideal space charge region conditions and half filling of the intermediate band,” *J. Appl. Phys.*, vol. 99, no. 9, pp. 094503-1–094503-9, May 2006.

[6] L. A. A. Pettersson and L. S. Roman, “Modeling photocurrent action spectra of photovoltaic devices based on organic thin films,” *J. Appl. Phys.*, vol. 86, no. 1, pp. 487–496, Jul. 1999.

[7] A. Martí, L. Cuadra, and A. Luque, “Quasi-drift diffusion model for the quantum dot intermediate band solar cell,” *IEEE Trans. Electron. Devices*, vol. 49, no. 9, pp. 1632–1639, Sep. 2002.

[8] T. Sugaya, S. Furue, O. Numakami, T. Amano, M. Mori, K. Komori, Y. Okano, and S. Niki, “Characteristics of highly stacked quantum dot solar cells fabricated by intermittent deposition of InGaAs,” in *Proc. IEEE 35th Photovoltaic Spec. Conf.*, Jun. 2010, pp. 1863–1867.

[9] C. G. Bailey, D. V. Forbes, R. P. Raffaelle, and S. M. Hubbard, “Near 1 V open circuit voltage InAs/GaAs quantum dot solar cells,” *Appl. Phys. Lett.*, vol. 98, no. 16, pp. 163105-1–163105-3, Apr. 2011.

[10] R. Oshima, A. Takata, Y. Shoji, K. Akahane, and Y. Okada, “InAs/GaNAs strain-compensated quantum dots stacked up to 50 layers for use in high-efficiency solar cell,” *Phys. E*, vol. 42, no. 10, pp. 2757–2760, Sep. 2010.

[11] M. Zeman, R. A. C. M. M. van Swaaij, and J. W. Metselaar, “Optical modeling of a-Si:H solar cells with rough interfaces: Effect of back contact and interface roughness,” *J. Appl. Phys.*, vol. 88, no. 11, pp. 6436–6443, Dec. 2000.

[12] G. F. Burkhard, E. T. Hoke, and M. D. McGehee, “Accounting for interference, scattering, and electrode absorption to make accurate internal quantum efficiency,” *Adv. Mater.*, vol. 22, no. 30, pp. 3293–3297, May 2010.

[13] A.-A. S. Al-Omar, “The collection probability and spectral response in isotype heterolayers of tandem solar cells,” *Solid-State Electron.*, vol. 50, no. 9–10, pp. 1656–1666, Sep.-Oct. 2006.

[14] T. Worren Reenaas, “Modeling of Intermediate Band Solar Cells” M.S. thesis, Dept. Phys., Norwegian Univ. Sci. Technol., 2009.

[15] A. Marti, L. Cuadra, and A. Luque, “Design constraints of the quantum-dot intermediate band solar cell,” *Phys., E.*, vol. 14, no. 1–2, pp. 150–157, Apr. 2002.

[16] S. L. Chuang, *Physics of Photonic Devices*. Hoboken, NJ, USA: Wiley, 2009, pp. 376–378.

[17] J. R. Guest, T. H. Stievater, Xiaoqin Li, Jun Cheng, D. G. Steel, D. Gammon, D. S. Katzer, D. Park, C. Ell, A. Thrauhardt, G. Khitrova, and H. M. Gibbs, “Measurement of optical absorption by a single quantum dot exciton,” *Phys. Rev. B*, vol. 65, no. 24, pp. 1–4, Jun. 2002.

[18] W. G. Hu, T. Inoue, O. Kojima, and T. Kita, “Effects of absorption coefficients and intermediate-band filling in InAs/GaAs quantum dot solar cells,” *Appl. Phys. Lett.*, vol. 97, no. 19, pp. 193106-1–193106-3, Nov. 2010.

[19] S.-C. Lee, “Epitaxial Growth of GaNAs Material and Study of Wet Oxidation of AlAs” M.S. thesis, Dept. Electro-Phys., Nat. Chiao Tung Univ., 2001.

[20] A. S. Lin, “*Modeling of Solar Cell Efficiency Improvement Using Optical Gratings and Intermediate Absorption Band*” Ph.D. dissertation, Dept. Elect. Eng., The University of Michigan, 2010.

[21] T. Sugaya, O. Numakami, S. Furue, H. Komaki, T. Amano, K. Komori, K. Matsubara, Y. Okano, and S. Niki, “Ultra-high stacks of InGaAs quantum dots for high efficiency solar cells,” in *Proc. IEEE 37th Photovoltaic Spec. Conf.*, 2011, pp. 002661–002664.

[22] Y. Okada, R. Oshima, and A. Takata, “Characteristics of InAs/GaNAs strain-compensated quantum dot solar cell,” *J. Appl. Phys.*, vol. 106, pp. 024306-1–024306-3, 2009.

[23] C. G. Bailey, S. M. Hubbard, D. V. Forbes, and R. P. Raffaelle, “Evaluation of strain balancing layer thickness for InAs/GaAs quantum dot arrays using high resolution X-ray diffraction and photoluminescence,” *Appl. Phys. Lett.*, vol. 95, pp. 203110-1–203110-3, 2009.

[24] V. Popescu, G. Bester, M. C. Hanna, A. G. Norman, and A. Zunger, “Theoretical and experimental examination of the intermediate-band concept for strain-balanced (In, Ga) As/Ga (As, P) quantum dot solar cells,” *Phys. Rev. B*, vol. 78, no. 20, pp. 205321-1–205321-17, 2008.

[25] P. G. Linares, A. Martí, E. Antolín, C. D. Farmer, Í. Ramiro, C. R. Stanley, and A. Luque, “Voltage recovery in intermediate band solar cells,” *Solar Energy Mater. Solar Cells*, vol. 98, pp. 240–244, 2011.

[26] S. Hubbard and R. Raffaelle. (2010, Feb. 8). “Boosting solar-cell efficiency with quantum-dot-based nanotechnology,“ *SPIE Newsroom*. [Online]. Available: http://spie.org/x39022.xml

[27] E. Antolin, A. Marti, C. D. Farmer, P. G. Linares, E. Hernandez, A. M. Sanchez, T. Ben, S. I. Molina, C. R. Stanley, and A. Luque, “Reducing carrier escape in the InAs/GaAs quantum dot intermediate band solar cell,” *J. Appl. Phys.*, vol. 108, pp. 064513-1–064513-7, 2010.

[28] T. Sugaya, O. Numakami, S. Furue, H. Komaki, T. Amano, K. Matsubara, Y. Okano, and S. Niki, “Tunnel current through a miniband in InGaAs quantum dot superlattice solar cells,” *Solar Energy Mater. Solar Cells*, vol. 95, no. 10, pp. 2920–2923, 2011.

[29] K. Y. Chuang, T. E. Tzeng, Y. C. Liu, K. D. Tzeng, and T. S. Lay, “Photovoltaic response of coupled InGaAs quantum dots,” *J. Crystal Growth*, vol. 323, no. 1, pp. 508–510, May 2011.

[30] [Online]. Available:http://www.filmetrics.com/refractive-index-database, 2012, by Filmetrics, Inc.

[31] E. Antolín, A. Martí, P. G. Linares, I. Ramiro, and E. Hernández, “Advances in quantum dot intermediate band solar cells,” in *Proc. IEEE, IEEE 35th Photovoltaic Spec. Conf.*, Jun. 2010, pp. 65–70.

[32] R. T. Chen, D. P. Robinson, and R. Shih, “Single mode optically-activated phase modulator on GaAs/GaAlAs compound semiconductor channel waveguides,” *SPIE*, vol. 1794, no. 101, pp. 101–116, Apr. 1991.

[33] K. A. Bertness, S. R. Kurtz, D. J. Friedman, A. E. Kibbler, C. Kramer, and J. M. Olson, “29.5% efficient GaInP/GaAs tandem solar cells,” *Appl. Phys. Lett.*, vol. 65, no. 8, pp. 989–991, Aug. 1994.

[34] T. Takamoto, E. Ikeda, and H. Kurita, “Over 30% efficient InGaP/GaAs tandem solar cells,” *Appl. Phys. Lett.*, vol. 70, no. 3, pp. 381–383, Jan. 1997.

[35] T. Sugaya, A. Takeda, R. Oshima, K. Matsubara, S. Niki, and Y. Okano, “InGaP-based InGaAs quantum dot solar cells with GaAs spacer layer fabricated using solid-source molecular beam epitaxy,” *Appl. Phys. Lett.*, vol. 101, no. 13, pp. 133110-1–133110-4, Sep. 2012.

[36] M. J. Griggs, D. C. Law, R. R. King, A. C. Ackerman, J. M. Zahler, and H. A. Atwater, “Design approaches and materials progress for ultrahigh efficiency lattice mismatched multi-junction solar cells,” in *Proc. Conf. Rec. 2006 IEEE 4th World Conf. Photovoltaic Energy Convers.*, May 2006, pp. 857–860.

[37] J. F. Geisz, S. Kurtz, M. W. Wanlass, J. S. Ward, A. Duda, D. J. Friedman, J. M. Olson, W. E. McMahon, T. E. Moriarty, and J. T. Kiehl, “High-efficiency GaInP/GaAs/InGaAs triple-junction solar cells grown inverted with a metamorphic bottom junction,” *Appl. Phys. Lett.*, vol. 91, no. 2, p. 023502, Jul. 2007.

[38] C. H. Henry, “Limiting efficiencies of ideal single and multiple energy gap terrestrial solar cells,” *J. Appl. Phys.*, vol. 51, no. 8, pp. 4494–4500, Aug. 1980.

[39] S. R. Kurtz, P. Faine, and J. M. Olson, “Modeling of two-junction, series-connected tandem solar cells using top-cell thickness as an adjustable parameter,” *J. Appl. Phys.*, vol. 68, no. 4, pp. 1890–1895, Aug. 1990.

Chien-Chung Lin was born in Taipei, Taiwan, in 1970. He received the B.S. degree in electrical engineering from the National Taiwan University, Taipei, in 1993, and the M.S. and Ph.D. degrees in electrical engineering from Stanford University, Stanford, CA, in 1997 and 2002, respectively. His thesis was in the field ofdesign, modeling, and fabrication of micromachined tunable optoelectronic devices.

He has been with the National Chiao Tung University (NCTU), Tainan, Taiwan, since 2009, where he holds a position as an Assistant Professor. The major research efforts in his group are in design and fabrication of semiconductor optoelectronic devices, including light emitting diodes, solar cells, and lasers. Before joining NCTU, he was with different start-ups in the United States. After graduating from Stanford in 2002, he joined E2 O Communications, Inc., Calabasas, CA, USA, as a Senior Optoelectronic Engineer. In 2004, he joined Santur Corporation, Fremont, CA, USA, where he initially worked as a Member of theTechnical Staff then became a Manager of laser chip engineering. He had worked on various projects such as monolithic multiwavelength distributed feedback (DFB) laser arrays for data and telecommunications applications and yield and reliability analysis of DFB laser arrays. He has more than 40 journal papers and numerous conference publications.

Dr. Lin is a member of the IEEE Photonic Society and the Electron Devices Society.

Ming-Hsuan Tan received the B.S. degree in engineering and system science from National Tsing Hua University, Hsinchu, Taiwan, in 2011. He is currently working toward the M.S. degree in photovoltaic systems from National Chiao Tung University, Tainan, Taiwan. The interest of his master studies includes quantum dot intermediate band solar cell simulation and optimization of thin-film solar cell and tandem cell.

Che-Pin Tsai received the B.S. degree in materials and optoelectronic science from National Sun Yat-Sen University, Kaohsiung, Taiwan, in 2011. He is currently working toward the M.S. degree in photovoltaic systems from National Chiao Tung University, Tainan, Taiwan.

His current research interests include quantum dot intermediate band solar cell simulation and process optimization.

Kuei-Ya Chuang was born in Chiayi, Taiwan, in 1979. She recived the B.S. degree in electric engineering from I-Shou University, Kaohsiung, Taiwan, and the Master's and Ph.D. degrees in photonics from National Sun Yat-Sen University, Kaohsiung, Taiwan.

After her graduation, she joined the Department of Electric Engineering as a Postdoctoral Associate in National Chung Hsing University, Taichung, Taiwan. Her research interests include vertically coupled InGaAs quantum dot.

T. S. Lay (M'03) was born in Taiwan in 1964. He received the B.S. and M.S. degrees in electrical engineering from National Taiwan University, Taipei, Taiwan, and the Ph.D. degree in electrical engineering in 1996 from Princeton University, Princeton, NJ, USA, where his research activities were in the field ofmagneto-transport and phase transitions of fractional quantum Hall states in coupled 2-D electron systems.

In 1996, he became a Faculty Member in National Sun Yat-Sen University. He was a Professor, the Director, and the Chairman in the Department of Photonics, Institute of Electro-Optical Engineering. Since 2012 summer, he has been a Professor in the Department of Electrical Engineering, National Chung Hsing University, Taichung, Taiwan. He also served as the Chair for the IEEE Photonics Society Taipei Chapter (2011–2012). His current research interests include the optoelectronic devices and physics based on semiconductor quantum structures, molecular beam epitaxy, and nanophotonics.

Dr. Lay is a member of the IEEE Photonics Society and Electron Devices Society.